Supplementary Material for "Solute Release from Floodplains during Distinct Types of Inundation Events: Insights from Field Experiments and Reactive Transport Simulations"

Zach Perzan[1], Kristin Boye[2], John R. Bargar[3], and Kate Maher[4]

[1]Department of Geoscience, University of Nevada Las Vegas, Las Vegas, NV, USA
[2]SLAC National Accelerator Laboratory, Menlo Park, CA, USA
[3]Environmental Molecular Science Laboratory, Pacific Northwest National Laboratory, Richland, WA, USA
[4]Department of Earth System Science, Stanford University, Stanford, CA, USA

Correspondence: Zach Perzan (zach.perzan@unlv.edu)

S1 Governing equations within MIN3P

S1.1 Variably saturated flow

Dual-permeability water flow and solute transport within MIN3P are represented using two continua, with separate hydraulic and transport parameters assigned to each domain. Variably saturated water flow in each domain is described using the Richards equation:

$$S_{w,\mathrm{mat}} S_{s,\mathrm{mat}} \frac{\partial \psi_{\mathrm{mat}}}{\partial t} + \phi_{\mathrm{mat}} \frac{\partial S_{w,\mathrm{mat}}}{\partial t} - \nabla \cdot [K_{\mathrm{mat}}(\psi_{\mathrm{mat}}) \nabla \psi_{\mathrm{mat}}] + Q_{a,\mathrm{mat}} - \Gamma_w = 0, \tag{1}$$

$$S_{w,\mathrm{mac}} S_{s,\mathrm{mac}} \frac{\partial \psi_{\mathrm{mac}}}{\partial t} + \phi_{\mathrm{mac}} \frac{\partial S_{w,\mathrm{mac}}}{\partial t} - \nabla \cdot [K_{\mathrm{mac}}(\psi_{\mathrm{mac}}) \nabla \psi_{\mathrm{mac}}] + Q_{a,\mathrm{mac}} + \Gamma_w = 0, \tag{2}$$

where the subscripts $_{\mathrm{mat}}$ and $_{\mathrm{mac}}$ represent the matrix and macropore domains, respectively; S_w is water saturation; S_s is specific storage; ψ is hydraulic head; phi is porosity, K_ψ is the unsaturated hydraulic conductivity at a given head, and $Q_{a,d}$ represents external water sources or sinks, such as root water uptake. Water transfer between the macropores and soil matrix, Γ_w, is represented using the first-order approximation of Gerke and Van Genuchten (1993a):

$$\Gamma_w = \frac{\beta}{\alpha^2} \gamma_w K_a \left(\psi_{\mathrm{mac}} - \psi_{\mathrm{mat}}\right), \tag{3}$$

where β is a geometry factor that describes the shape of soil aggregates between the macropores; α represents the characteristic length from the center of a matrix block to the edge of a macropore; γ_w is an empirical scaling coefficient; and K_a is the unsaturated hydraulic conductivity of the macropore–matrix interface. As written above, positive Γ_w denotes transfer from the macropores to the soil matrix.

S1.2 Solute transport

Aqueous species are transported separately through the macropores and soil matrix by advection and dispersion, while reactions and mass transfer between the two domains are represented explicitly. For aqueous species j, the mass balance equations within each domain are:

$$\frac{\partial}{\partial t}\left(S_{w,\mathrm{mac}}\phi_{\mathrm{mac}}C_{j,\mathrm{mac}}\right)+\nabla\cdot\left(\mathbf{q}_{\mathrm{mac}}C_{j,\mathrm{mac}}\right)-\nabla\cdot\left(S_{w,\mathrm{mac}}\phi_{\mathrm{mac}}\mathbf{D}_{\mathrm{mac}}\nabla C_{j,\mathrm{mac}}\right)-Q^{\mathrm{in}}_{j,\mathrm{mac}}-Q^{\mathrm{ext}}_{j,\mathrm{mac}}+\Gamma_j=0, \tag{4}$$

$$\frac{\partial}{\partial t}\left(S_{w,\mathrm{mat}}\phi_{\mathrm{mat}}C_{j,\mathrm{mat}}\right)+\nabla\cdot\left(\mathbf{q}_{\mathrm{mat}}C_{j,\mathrm{mat}}\right)-\nabla\cdot\left(S_{w,\mathrm{mat}}\phi_{\mathrm{mat}}\mathbf{D}_{\mathrm{mat}}\nabla C_{j,\mathrm{mat}}\right)-Q^{\mathrm{in}}_{j,\mathrm{mat}}-Q^{\mathrm{ext}}_{j,\mathrm{mat}}-\Gamma_j=0, \tag{5}$$

where C_j is the total aqueous concentration of species j, $\mathbf{q}$ is the specific discharge, $\mathbf{D}$ is the hydrodynamic dispersion tensor, $Q^{\mathrm{in}}_{j,d}$ represents internal sources and sinks associated with aqueous reactions, mineral dissolution–precipitation, and other geochemical processes; and $Q^{a,\mathrm{ext}}_{j,d}$ represents solute sources or sinks, such as from root water uptake. The solute mass transfer term (Γ_j) accounts for both advective and diffusive fluxes (Gerke and Van Genuchten, 1993a):

$$\Gamma_j=\frac{\beta}{\alpha^2}(1-\omega)S_{w,\mathrm{mat}}\phi_{\mathrm{mat}}\mathbf{D}_{\mathrm{ex}}\left(C_{j,\mathrm{mac}}-C_{j,\mathrm{mat}}\right)+\Gamma_w C^*_j \tag{6}$$

where ω is the fraction of the bulk soil volume occupied by macropores, $\mathbf{D}^a_{\mathrm{ex}}$ is the effective molecular diffusion coefficient of the matrix near the matrix–macropore interface, and C^*_j is the upstream concentration of species j, depending on whether water is being transferred from the macropores to the matrix or vice versa. A more complete description of the governing equations can be found elsewhere (Gerke and Van Genuchten, 1993a; Gerke and van Genuchten, 1993b; Jia et al., 2023).

S2 Supplementary figures

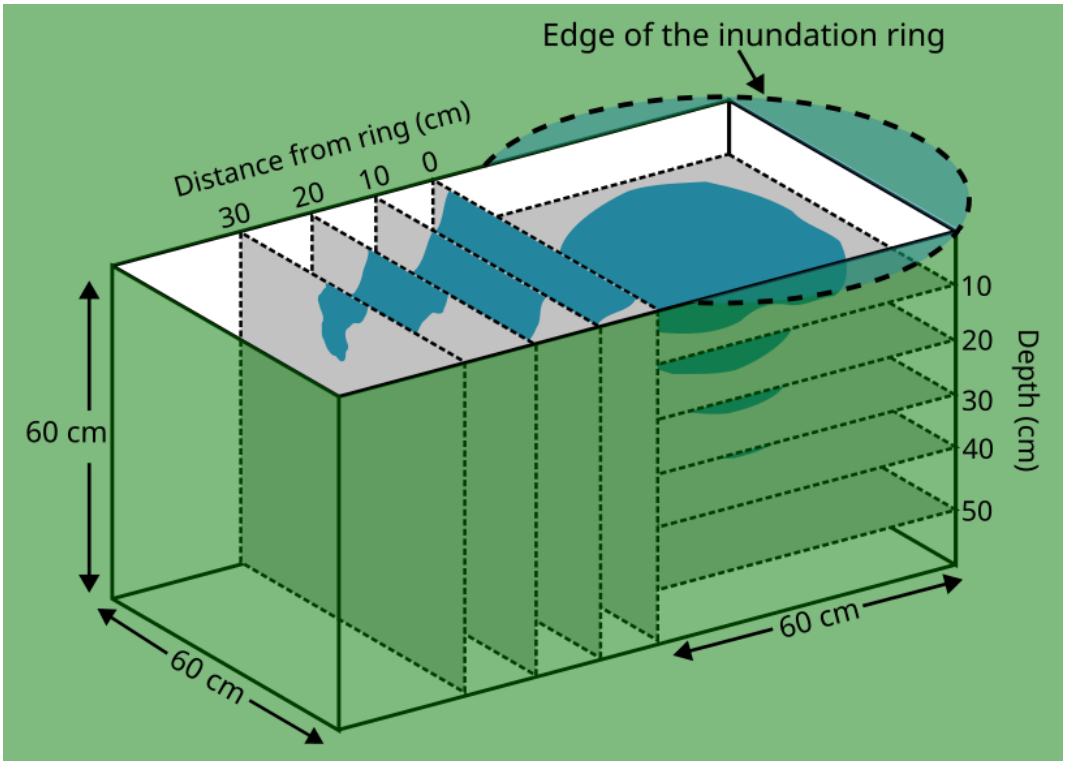

Figure S1. Diagram of the horizontal and vertical cross-sections used to excavate the soil profile following the dye tracer test. Note that the soil pit was excavated down to 145 cm, though only the upper 60 cm is shown here.

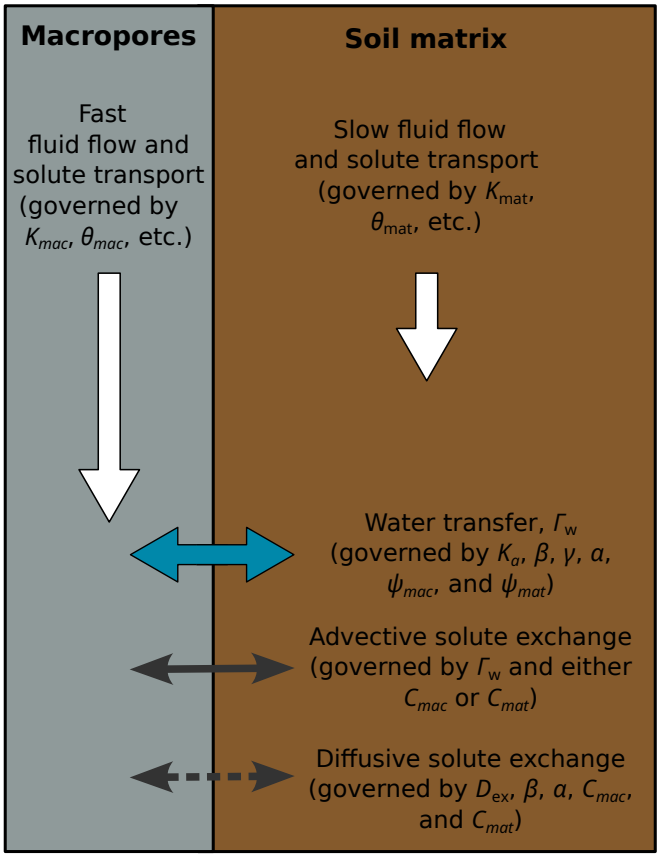

Figure S2. Diagram of the implementation of dual permeability flow and solute transport in MIN3P, as well as the major parameters that govern fluxes between each domain.

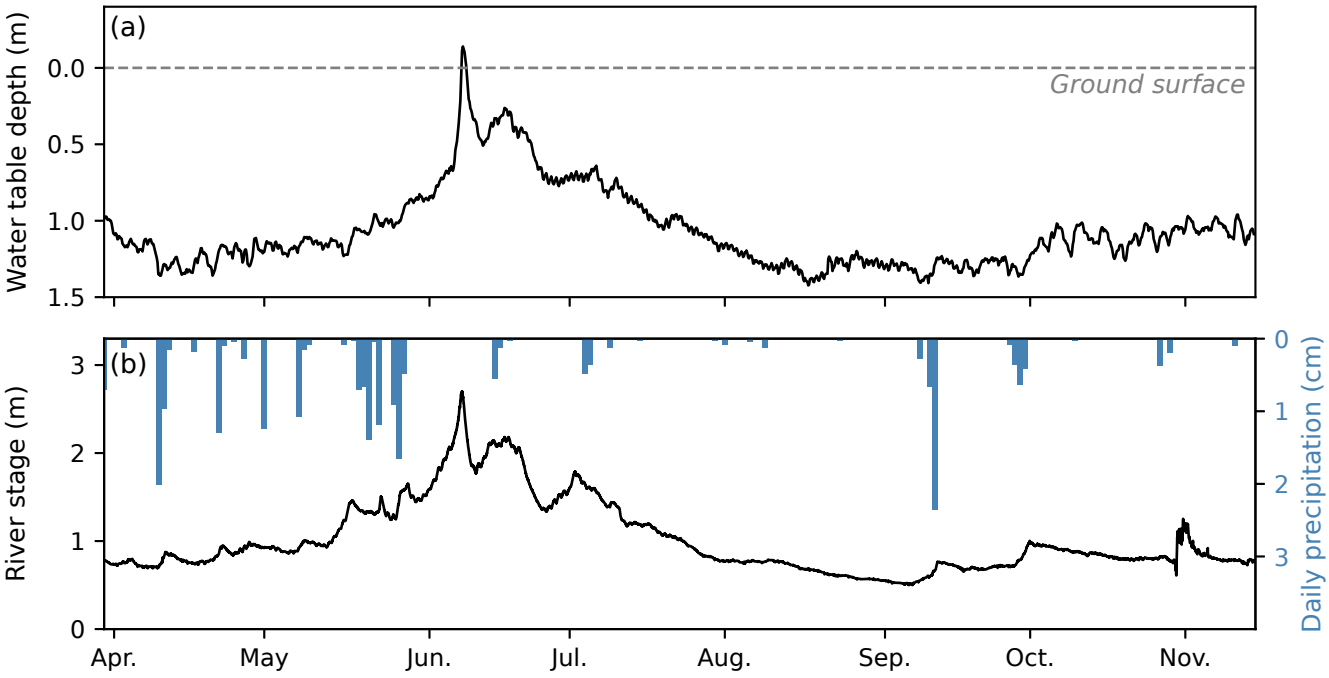

Figure S3. Comparison of water table depth within the floodplain (a) to river stage at a streamgage 4 km downstream (b). Both time series exhibit similar trends, indicative of the hydrologic connection between the river and the floodplain aquifer.

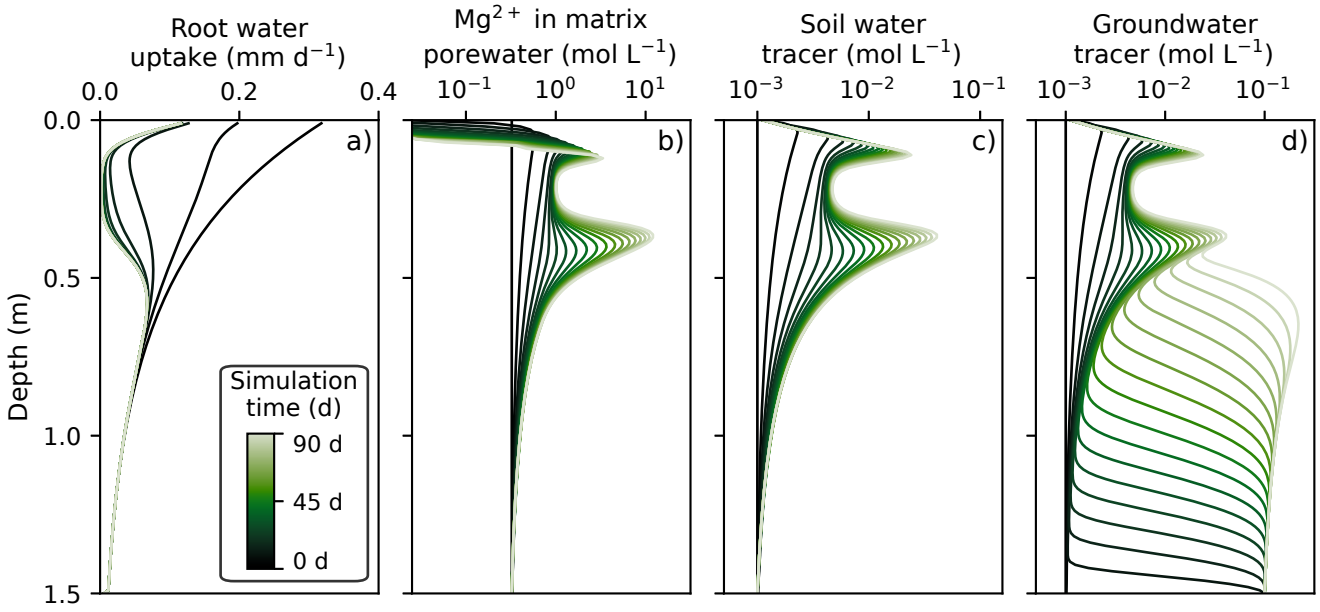

Figure S4. hanges in root water uptake (a), porewater Mg^{2+} (b), and tracer concentrations (c–d) during the spin-up period. Initial and boundary conditions for the soil water tracer are set to 10^{-3} $\mathrm{mol\,L^{-1}}$; all changes in concentration are due to evaporative concentration of soil porewater. Initial concentrations of the groundwater tracer are 10^{-3} $\mathrm{mol\,L^{-1}}$, while the bottom boundary is 10^{-1} $\mathrm{mol\,L^{-1}}$; these profiles demonstrate both upward flow of groundwater into the soil, as well as evaporative concentration of the groundwater tracer in soil porewater.

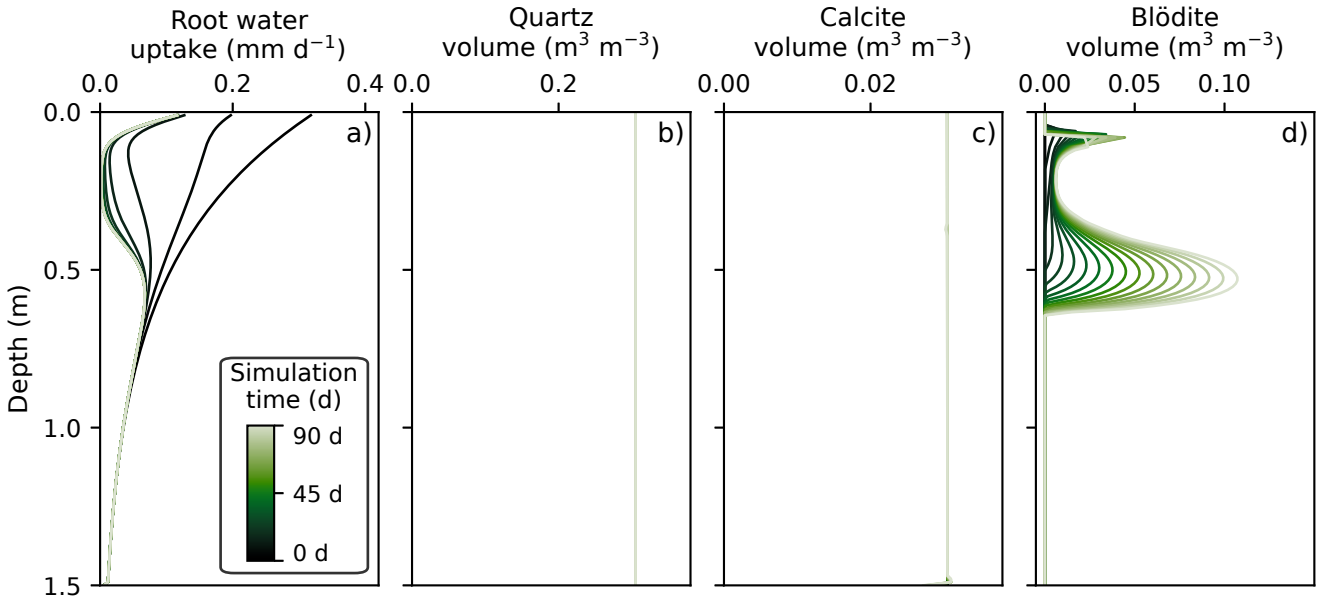

Figure S5. Changes in root water uptake (a) and mineral volume fractions (b–d) during the spin-up period. Minimal changes occur in the distribution of quartz and calcite, while extensive blödite precipitation can be observed in the top 60 cm of the soil.

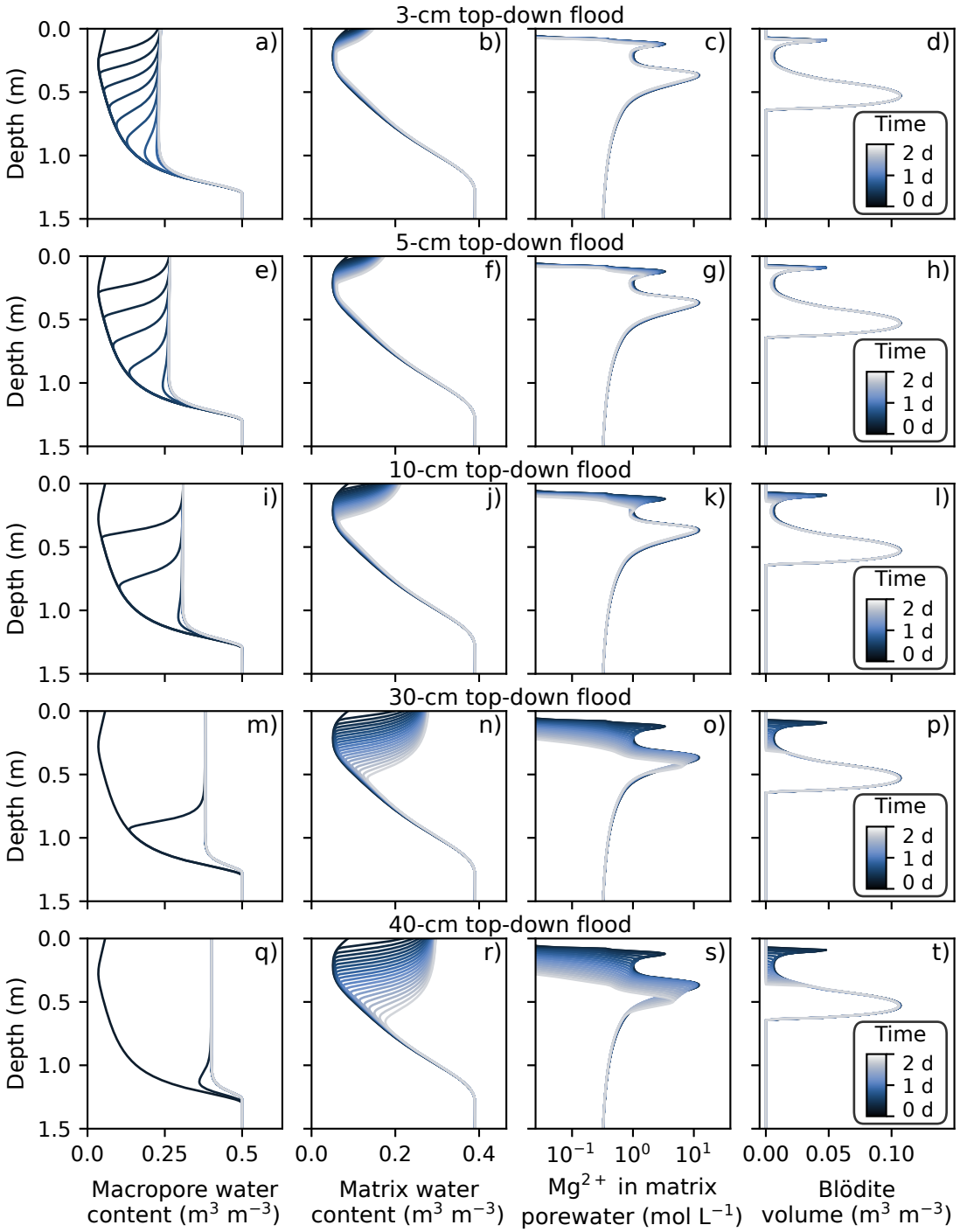

Figure S6. Changes in macropore water content, soil matrix water content, porewater Mg^{2+}, and blödite volume during 5 top-down floods of varying intensities. Lines are plotted every 0.1 d.

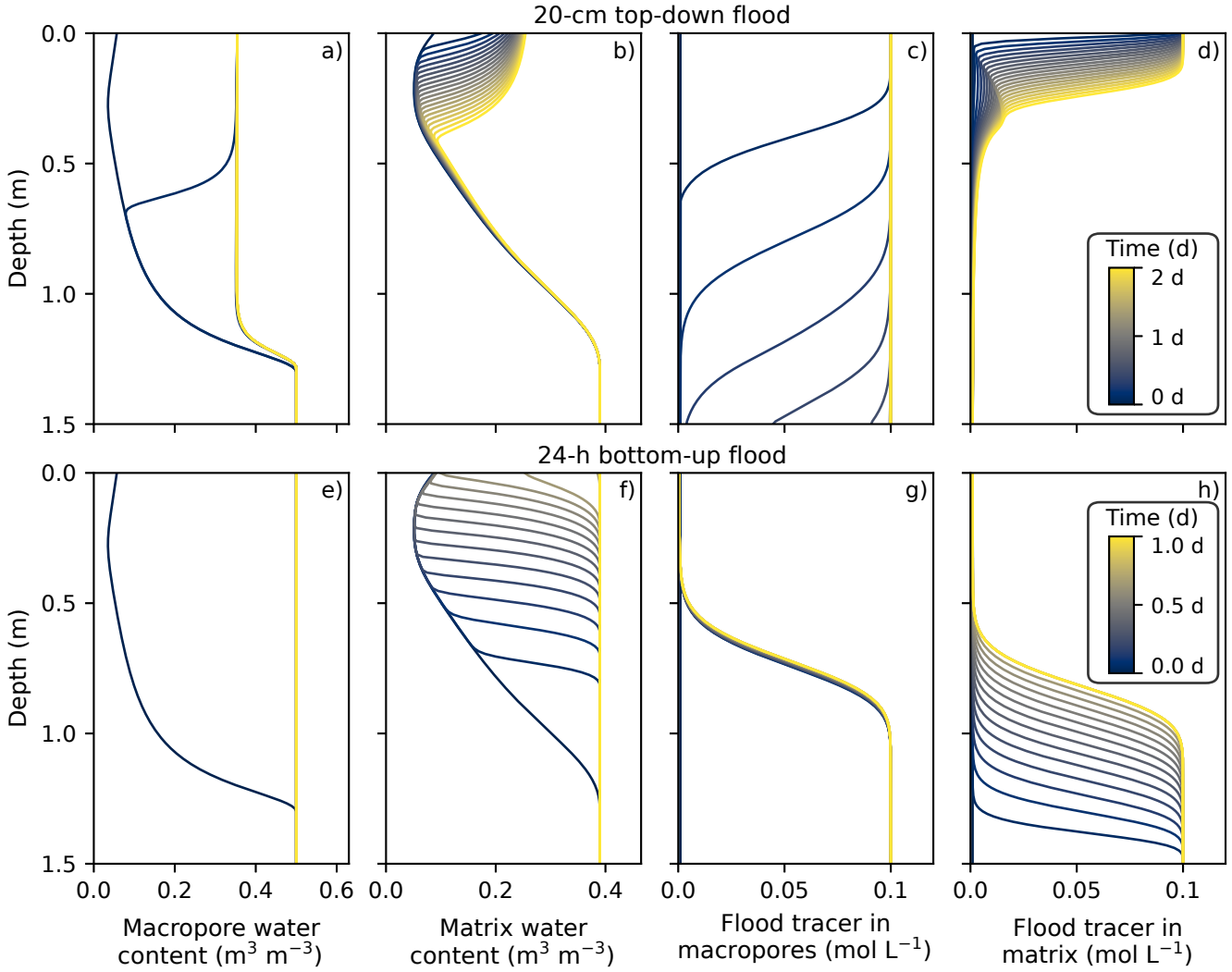

Figure S7. Profiles of water content in the soil matrix, root water uptake, and tracer concentrations during a 20-cm top-down flood (a–d) and a 24-h bottom-up flood (e–h). For the top-down flood, tracer infiltrates from the surface and for the bottom-up flood, tracer advects upward from the bottom boundary.

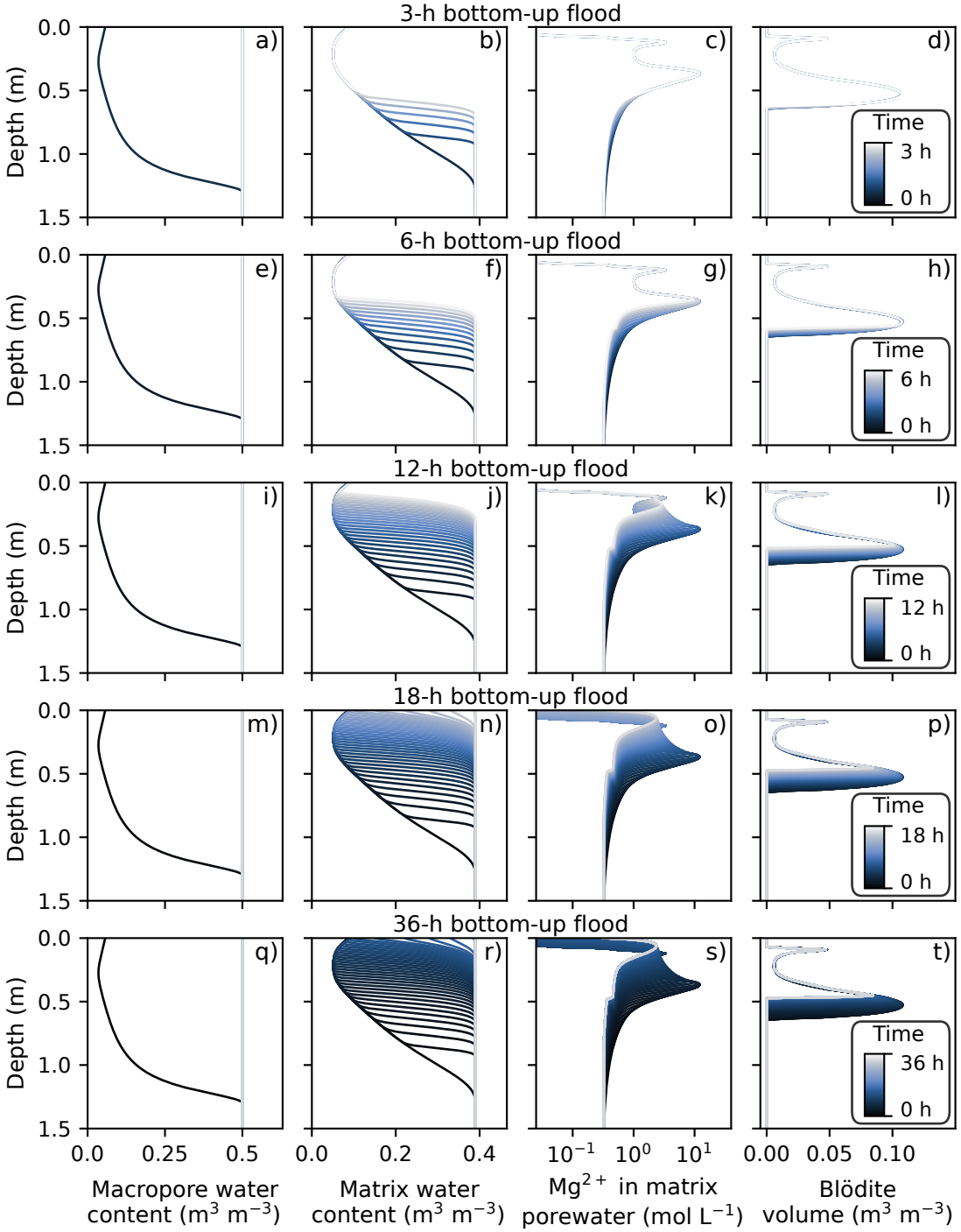

Figure S8. Changes in macropore water content, soil matrix water content, porewater Mg^{2+}, and blödite volume during 5 bottom-up floods of varying intensities. Lines are plotted every 0.5 h.

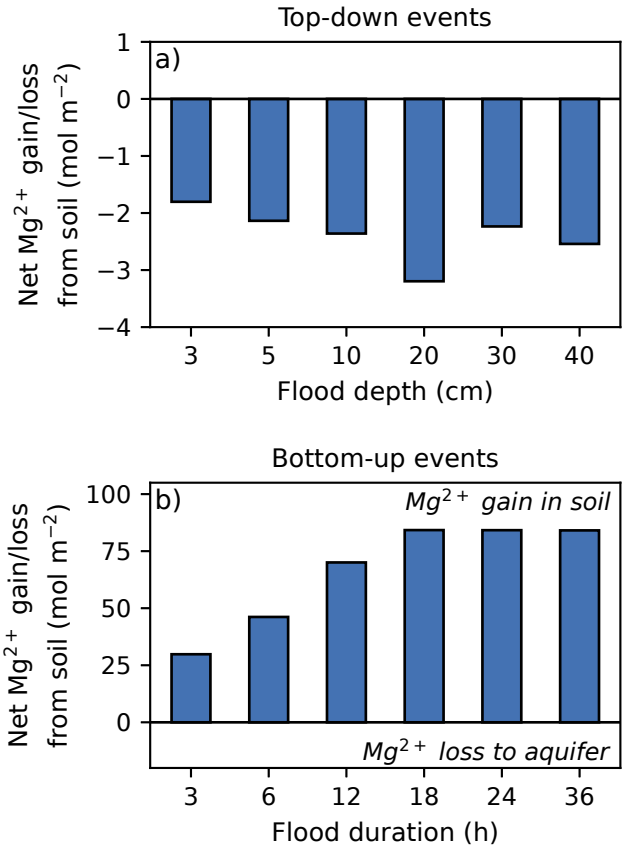

Figure S9. Net gain or loss of Mg^{2+} from the soil to the underlying aquifer for both top-down (a) and bottom-up (b) flood scenarios. Net solute exchange was calculated across a control plane at 1.3 m depth and negative values represent net solute losses from the soil to the aquifer.

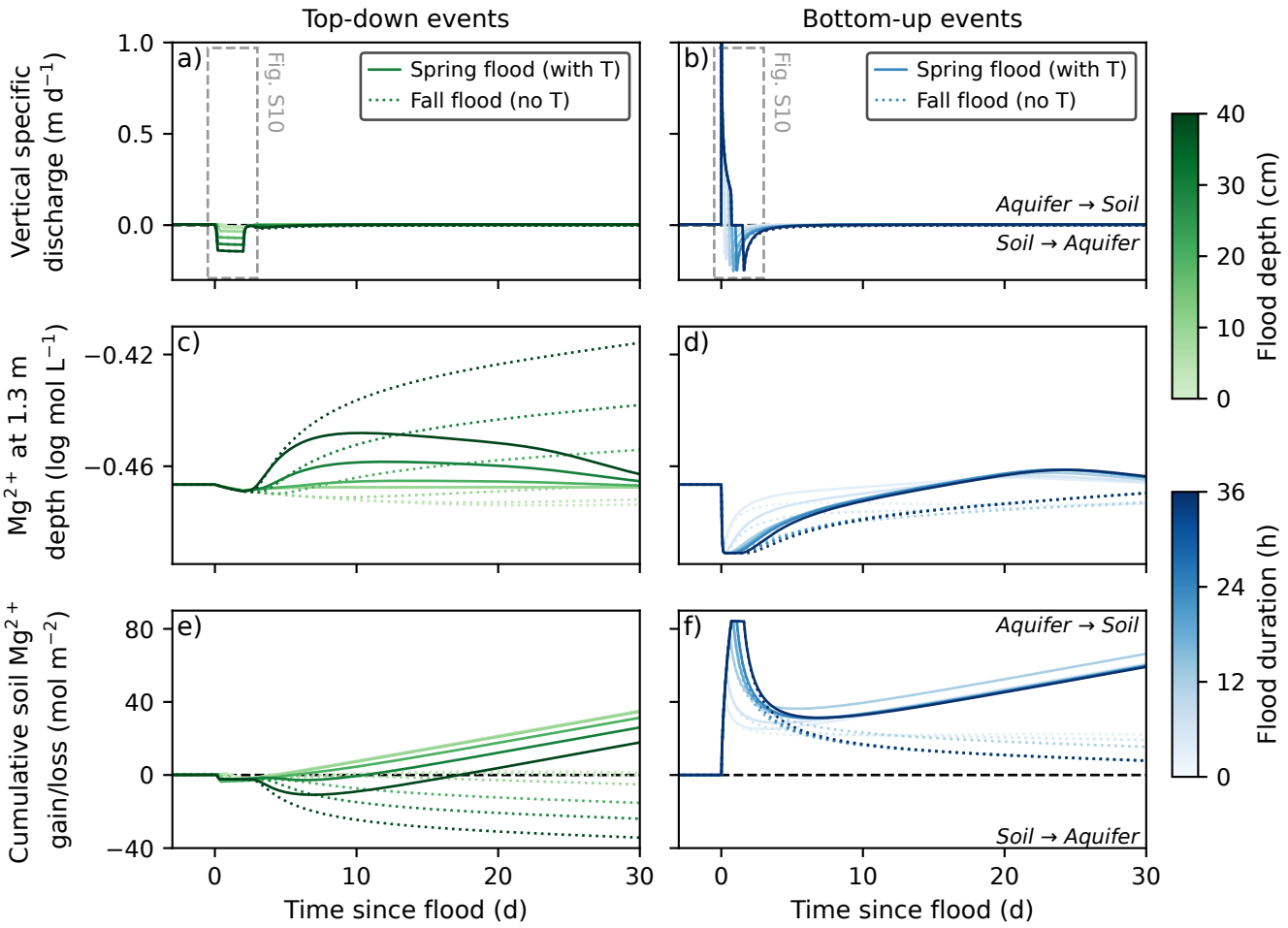

Figure S10. Changes in vertical specific discharge, Mg^{2+} concentrations in the soil matrix, and cumulative Mg^{2+} flux across a control plane at 1.3 m depth for 30 d following each top-down and bottom-up inundation event. To better visualize the rapid changes in specific discharge during each event, the insets from (a) and (b) are shown in Fig. S11.

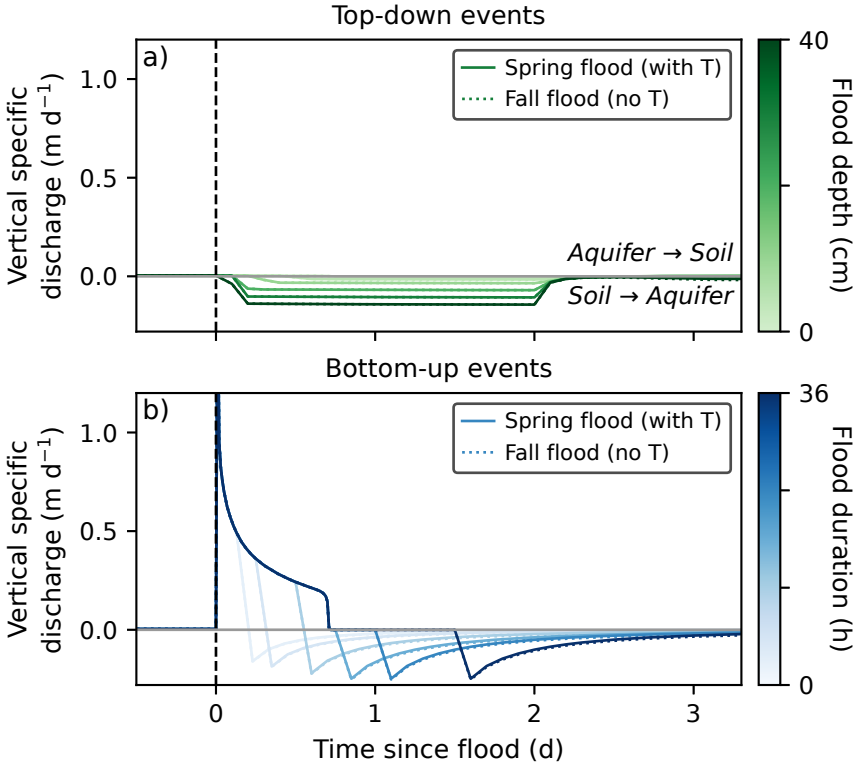

Figure S11. Changes in vertical specific discharge across a control plane at 1.3 m depth during and immediately following each top-down (a) and bottom-up (b) inundation event.

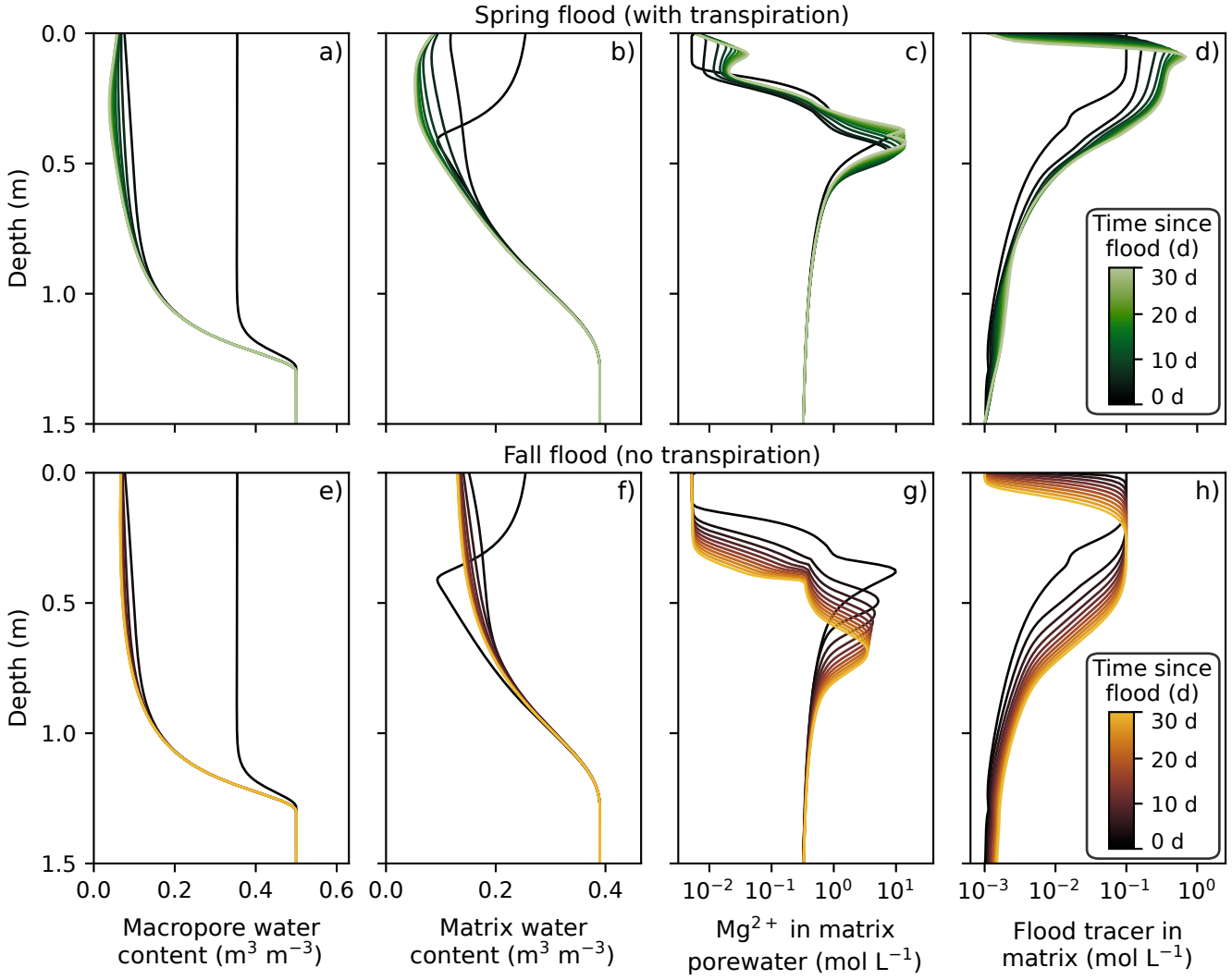

Figure S12. Changes in macropore water content, soil matrix water content, Mg^{2+} in matrix porewater, and the flood tracer in matrix porewater following a spring top-down flood (a–d) and a fall top-down flood (e–h). Both simulations follow the 20-cm top-down flood shown in Fig. 6a–d. Lines are plotted every 5 d.

S3 Supplementary tables

Table S1. Soil hydraulic function parameters for both the soil matrix and the soil macropores

Parameter	Matrix	Macropores
Sat. hydraulic conductivity (m/s)	4.3889 $\times 10^{-6}$	2.3148 $\times 10^{-4}$
Porosity (m^3/m^3)	0.39	0.5
Residual water content (m^3/m^3)	0.039	0.0
van Genuchten α (m^{-1})	2.69	10.0
van Genuchten n	2.45	2.0

Table S2. Parameters used to describe dual permeability flow according to Gerke and Van Genuchten (1993a)

Parameter[a]	Value
Geometry shape factor (β)	3.0
Scaling factor (γ_w)	0.4
Effective diffusion path length (a)	0.01 m
Effective diffusion coefficient at interface (D_a)	5×10^{-9} $\mathrm{m^2 s^{-1}}$
Effective hydraulic conductivity of interface (K_a)	2.315×10^{-6} $\mathrm{m\ s^{-1}}$

[a]See Text S1 for a detailed discussion of each term.

Table S3. Stoichiometry and equilibrium constants for all equilibrium reactions.

Reaction	log K[a] (at 25°C)
$CaCl^+ \rightleftharpoons Ca^{2+} + Cl^-$	-0.4
$CaCO_3(aq) \rightleftharpoons Ca^{2+} + CO_3^{2-}$	-3.2
$CaHCO_3^+ \rightleftharpoons Ca^{2+} + CO_3^{2-} + H^+$	-11.599
$CaOH^+ + H^+ \rightleftharpoons Ca^{2+} + H_2O$	12.697
$CaSO_4(aq) \rightleftharpoons Ca^{2+} + SO_4^{2-}$	-2.36
$HCO_3^- \rightleftharpoons CO_3^{2-} + H^+$	-10.329
$HSO_4^- \rightleftharpoons SO_4^{2-} + H^+$	-1.99
$H_2CO_3(aq) \rightleftharpoons CO_3^{2-} + 2H^+$	-16.681
$H_2SiO_4^{2-} + 2H^+ \rightleftharpoons H_4SiO_4$	23.04
$H_3SiO_4^- + H^+ \rightleftharpoons H_4SiO_4$	9.84
$MgCO_3(aq) \rightleftharpoons Mg^{2+} + CO_3^{2-}$	-2.92
$MgHCO_3^+ \rightleftharpoons Mg^{2+} + CO_3^{2-} + H^+$	-11.339
$MgSO_4(aq) \rightleftharpoons Mg^{2+} + SO_4^{2-}$	-2.26
$NaCO_3^- \rightleftharpoons Na^+ + CO_3^{2-}$	-1.27
$NaHCO_3(aq) \rightleftharpoons Na^+ + CO_3^{2-} + H^+$	-10.079
$NaSO_4^- \rightleftharpoons Na^+ + SO_4^{2-}$	-0.73
$H_2O \rightleftharpoons OH^- + H^+$	-13.997
$CO_2(g) + H_2O \rightleftharpoons CO_3^{2-} + 2H^+$	-18.147

[a]All equilibrium constants are from the Visual MINTEQ v4.0 database.

Table S4. Stoichiometry and equilibrium constants for mineral precipitation–dissolution reactions

Mineral	Reaction stoichiometry	log K (at 25 °C)
Quartz	$SiO_2(s) + H_2O \rightleftharpoons H_4SiO_4(aq)$	-4.0[a]
Calcite	$CaCO_3(s) \rightleftharpoons Ca^{2+} + CO_3^{2-}$	-8.48[a]
Gypsum	$CaSO_4 \cdot 2H_2O \rightleftharpoons Ca^{2+} + SO_4^{2-} + 2H_2O$	-4.61[a]
Blödite	$Na_2Mg(SO_4)_2 \cdot 4H_2O \rightleftharpoons 2Na^{+} + Mg^{2+} + 2SO_4^{2-} + 4H_2O$	-2.35[b]

[a]Visual MINTEQ v4.0

[b]From Harvie et al. (1984).

Table S5. Reactive surface area and rate constants for mineral precipitation–dissolution reactions

Mineral	Specific surface area[a] ($m^2\ g^{-1}$)	Rate constant [log (mol $m^{-2}\ s^{-1}$)]
Quartz	0.06[b]	-13.39[c]
Calcite	0.043[e]	-5.81[c]
Gypsum	0.096[d]	-2.79[c]
Blödite	0.1[f]	-0.21[g]

[a] Specific surface area was converted to bulk surface area ($m^2\ L^{-1}$ porous medium) using mineral densities and volume fractions.

[b] From Parks (1990), assuming a mean grain size of 50 μm.

[c] From Palandri and Kharaka (2004).

[d] Brunauer-Emmett-Teller (BET) surface area measured by Tang et al. (2018) and decreased by one order of magnitude to account for internal (non-reactive) surface area (Jeschke et al., 2001).

[f] Data unavailable.

[g] From Suarez and Wood (1984).

[g]Rate constants for blödite dissolution were unavailable, so kinetic parmaeters for halite were used instead (Palandri and Kharaka, 2004)

Table S6. Initial solute and mineral concentrations prior to the spin-up period.

Species	Concentration
pH	7.01
Na^+	9.57 $\times 10^{-1}$ mol/L
Mg^{2+}	7.86 $\times 10^{-1}$ mol/L
Ca^{2+}	7.84 $\times 10^{-4}$ mol/L
$SiO_2(aq)$	3.24 $\times 10^{-5}$ mol/L
CO_3^{2-}	1.46 $\times 10^{-2}$ mol/L
SO_4^{2-}	9.12 $\times 10^{-1}$ mol/L
Cl^-	1.47 $\times 10^{-1}$ mol/L
$Tracer_{sw}$[a]	1.00 $\times 10^{-3}$ mol/L
$Tracer_{gw}$[b]	1.00 $\times 10^{-3}$ mol/L
$Tracer_{fld}$[c]	1.00 $\times 10^{-3}$ mol/L
Quartz	0.3 m^3/m^3
Calcite	0.03 m^3/m^3
Gypsum	0.0061 m^3/m^3
Blödite	0.00001 m^3/m^3

[a] Inert tracer used to track evaporative concentration of soil porewater.

[b] Inert tracer used to track water from the underlying aquifer.

[c] Inert tracer used to track flood water.

Table S7. Concentrations of each primary species at the top and bottom boundaries.

Species	Top boundary[a]	Bottom boundary[a]
pH	7.01	7.01
Na^{+}	9.57×10^{-3}	9.57×10^{-1}
Mg^{2+}	7.86×10^{-3}	7.86×10^{-1}
Ca^{2+}	7.84×10^{-6}	7.84×10^{-4}
$\mathrm{SiO_2(aq)}$	3.24×10^{-7}	3.24×10^{-5}
$\mathrm{CO_3^{2-}}$	1.46×10^{-4}	1.46×10^{-2}
$\mathrm{SO_4^{2-}}$	9.12×10^{-3}	9.12×10^{-1}
Cl^{-}	1.47×10^{-3}	1.47×10^{-1}
$\mathrm{Tracer_{sw}}$	0.001	0.001
$\mathrm{Tracer_{gw}}$	0.001	0.1
$\mathrm{Tracer_{fld}}$	0.001[b]	0.001[c]

[a] All concentrations in $\mathrm{mol/L}$.

[b] Adjusted to 0.1 $\mathrm{mol/L}$ during top-down floods.

[c] Adjusted to 0.1 $\mathrm{mol/L}$ during bottom-up floods.

References

Gerke, H. H. and Van Genuchten, M. T.: A dual-porosity model for simulating the preferential movement of water and solutes in structured porous media, Water Resources Research, 29, 305–319, https://doi.org/10.1029/92WR02339, 1993a.

Gerke, H. H. and van Genuchten, M. T.: Evaluation of a first-order water transfer term for variably saturated dual-porosity flow models, Water Resources Research, 29, 1225–1238, https://doi.org/10.1029/92WR02467, 1993b.

Harvie, C. E., Møller, N., and Weare, J. H.: The prediction of mineral solubilities in natural waters: The Na-K-Mg-Ca-H-Cl-SO4-OH-HCO3-CO3-CO2-H2O system to high ionic strengths at 25°C, Geochimica et Cosmochimica Acta, 48, 723–751, https://doi.org/10.1016/0016-7037(84)90098-X, 1984.

Jeschke, A. A., Vosbeck, K., and Dreybrodt, W.: Surface controlled dissolution rates of gypsum in aqueous solutions exhibit nonlinear dissolution kinetics, Geochimica et Cosmochimica Acta, 65, 27–34, https://doi.org/10.1016/S0016-7037(00)00510-X, 2001.

Jia, M., Lapen, D. R., Su, D., and Mayer, K. U.: Modeling of dual-permeability gas and solute reactive transport in macroporous agricultural soils with a focus on GHG cycling and emissions, Journal of Hydrology, 620, 129 408, https://doi.org/10.1016/j.jhydrol.2023.129408, 2023.

Palandri, J. L. and Kharaka, Y. K.: A compilation of rate parameters of water-mineral interaction kinetics for application to geochemical modeling, Open File Report 2004-1068, U.S. Geological Survey, Menlo Park, CA, 2004.

Parks, G. A.: Surface energy and adsorption at mineral/water interfaces; an introduction, in: Reviews in Mineralogy and Geochemistry, vol. 23, pp. 133–175, GeoScienceWorld, https://pubs.geoscienceworld.org/msa/rimg/article/23/1/133/87264/Surface-energy-and-adsorption-at-mineral-water, 1990.

Suarez, D. L. and Wood, J. D.: Simultaneous Determination of Calcite Surface Area and Content in Soils, Soil Science Society of America Journal, 48, 1232–1235, https://doi.org/10.2136/sssaj1984.03615995004800060005x, 1984.

Tang, J., Bullard, J. W., Perry, L. N., Feng, P., and Liu, J.: An empirical rate law for gypsum powder dissolution, Chemical Geology, 498, 96–105, https://doi.org/10.1016/j.chemgeo.2018.09.013, 2018.